

# Custom-made optical scatterers produced by 3D direct laser writing

FELIX GLÖCKLER,<sup>1,\*</sup> DENNIS MÜLLER,<sup>1</sup> FREDERIKE ERB,<sup>2</sup> KAY-E. GOTTSCHALK<sup>2</sup> AND ALWIN KIENLE<sup>1</sup>

<sup>1</sup>*Institute for Lasertechnologies in Medicine and Metrology (ILM), Helmholtzstr. 12, 89081 Ulm, Germany*

<sup>2</sup>*Institute for Experimental Physics, Ulm University, 89081 Ulm, Germany*

\*[felix.gloeckler@ilm-ulm.de](mailto:felix.gloeckler@ilm-ulm.de)

**Abstract:** While 3D direct laser writing is a technique with growing popularity, there is little information about the quality of custom-made optical scatterers in current literature. The present work investigates a 3D direct laser writing system in view of its capability of producing micron scaled scatterers. Angular resolved scattering measurements on these scatterers are compared to numerical and analytical simulations proving the feasibility to produce elementary shaped particles with almost ideal shapes. Possible promising applications of these particles as scattering phantoms for biological samples are examined. Without the need for templates and molds, and production a cycle of less than a day, this method is ideally suited for the rapid prototyping of particle designs.

© 2019 Optical Society of America under the terms of the [OSA Open Access Publishing Agreement](#)

## 1. Introduction

Scattered light contains information about the shape [1], the size [2], the refractive index [3], and the inner structure [4] of the scatterer. As a label-free technique, light scattering measurements play an important role in investigating biological samples. These range from single spores [5], bacteria [6, 7], epithelial tissue [8] to live cells [4, 9, 10]. The scattered light can be observed e.g. spectrally [11, 12] as well as angularly [13, 14] resolved. Multimodal systems e.g. combine angularly and spectrally resolved measurements [15, 16].

Light scattering from microscopic single particles, such as cells and nuclei, was predominantly examined with Mie theory [17] which assumes all scatterers as spheres. For arbitrary geometries, computational hungry numerical methods, such as the Finite Difference Time Domain (FDTD) [18] or the Discrete Dipole Approximation (DDA) [19] method, have to be employed. To calibrate a light scattering system, measurements with controlled scatterers are an important tool. However, there are mainly spheroidal microparticles available on the market. Two of the most common materials for microparticles are polystyrene and silica. Polystyrene microparticles are used in various applications, such as drug carriers [20] or calibration material for particle counters [21], and can be produced by an emulsion polymerization process [22]. Silica microparticles are often used as model particle for biological samples [23] due to their relatively similar refractive index. They are produced by a sol-gel procedure described by Stöber *et al* [24]. Both materials can also be functionalized by chemical processes [25]. Spheroidal shaped microparticles can be produced by electrohydrodynamic co-jetting [26] or manipulating spherical particles [27]. Other shapes such as cubes [28], cylinders [28] and keyboard characters [29] can be produced using the hydrogel template method. All these methods are subjected to different limitations such as the achievable size, number or shape. Especially complex shapes, e.g. overhangs or partially hollow features are difficult to manufacture using the aforementioned methods.

In this work we investigated the possibilities of manufacturing scattering particles with arbitrary shape with a 3D direct laser writing system. Particles with elementary geometries were printed and examined with atomic force and scanning electron microscopy. After the examination of the particles' shape, light scattering experiments were conducted. The experimental results

were then compared to analytical and numerical simulations. As one possible application, the usage of these printed particles as light scattering phantoms for biological samples is demonstrated.

## 2. Methods

### 2.1. 3D direct laser writing (3D-DLW)

3D printing has already been successfully used to mimic biological tissue [30, 31] and with techniques such as the two-photon polymerization (2PP) it is possible to print objects with a resolution  $< 100$  nm [32]. 2PP is based upon ultrafast (e.g. femtosecond) pulsed lasers which are tightly focused into a photosensitive material, which polymerizes inside the focal region. Moving the focus of the beam in 3D through the material then allows the creation of three dimensional objects. The system used in the presented work is a commercially available 3D-DLW system, namely the Photonic Professional GT by Nanoscribe GmbH, Germany (see Fig. 1).

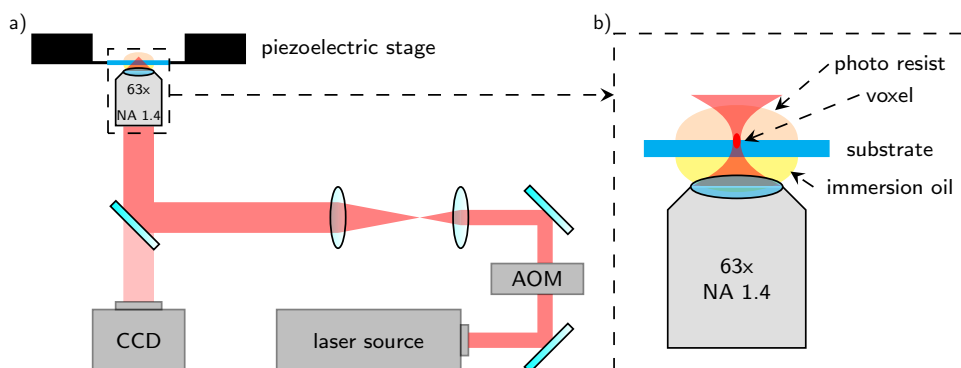


Fig. 1. **a)** Photonic Professional GT 3D-DLW system by Nanoscribe GmbH, Germany. On top of an inverted microscope a piezoelectric xyz-stage is mounted. The sample is illuminated by an erbium-doped fibre laser at  $\lambda = 780$  nm which produces 100 fs pulses at a repetition rate of 80 MHz. **b)** An objective lens with a high numerical aperture (NA = 1.4) tightly focuses the laser in a small volume (i.e. voxel). Here, the immersion lithography mode is depicted.

The 3D-DLW system consists of an inverted microscope on top of which a piezoelectric stage is mounted. The laser source is an erbium-doped fibre laser, which lases at 780 nm wavelength producing 100 fs pulses with a repetition rate of 80 MHz. The laser intensity is controlled by an acousto-optic modulator and tightly focused into the photo resist by an objective lens with high numerical aperture. The laser itself is adjusted to an average laser power of 50 mW at the 100% power setting. The printer can be operated with several different objectives depending on the targeted printing volume and purpose. Furthermore, the system can be operated in oil/air immersion or dip-in laser lithography (DiLL) mode, where the objective is dipped directly into the photo resist which then acts as an immersion medium. The printing process is done by either moving the sample or the focal spot of the laser. By moving the sample with the piezoelectric stage it is possible to produce complex micron-scale structures such as photonic crystals, however, the scan speed is usually below 100  $\mu\text{m/s}$ . An alternative, faster scan mode, where scan speeds up to 100.000  $\mu\text{m/s}$  are achievable, is performed by moving the focal spot with the galvo-mirrors (galvo scan mode) while the stage is fixed and only used for z-displacement (displacement along the optical axis). During this work the setup was used exclusively in the oil immersion lithography configuration and operated in galvo scan mode for fast model generation. Polymerization during

a 2PP process occurs in a very small but nonetheless finite volume which has, depending on the laser power, scan speed and the used objective, a lateral expansion in the range of hundreds of nanometres and usually an aspect ratio of height to lateral expansion  $>2$ . Thus, the size of the voxel affects the shape of the print, especially, if they are in the same order of magnitude. This had to be considered during the generation of the CAD-models. For the estimation of the voxel size or rather the line dimensions we used the results of Guney *et al* [33]. Although they operated their system in the DiLL configuration the results showed good agreement regarding the immersion lithography results of this work. For the immersion lithography IP-L 780 photoresist ( $n = 1.48$  at  $\lambda = 780$  nm) is drop-cast on a  $170 \mu\text{m}$  thick borosilica glass ( $n = 1.52$  at  $\lambda = 780$  nm) substrate. After the printing process the non-polymerized resist is dissolved with propylene glycol monomethyl ether acetate followed by cleaning the substrate and print with isopropyl alcohol and blow-drying it with canned air. No UV-curing procedure is required.

## 2.2. Scattering microscopy

The scattering microscope setup (see Fig. 2) and its evaluation has been thoroughly explained by Rothe *et al* [15]. Concisely, the system is an inverted microscope with darkfield illumination. The system's laser source is a supercontinuum laser (SuperK Blue, NKT Photonics A/S). To illuminate the sample with quasi-monochromatic light an acousto-optical tunable filter (AOTF, AOTF-PCAOM Vis, Crystal Technology) is introduced to the beam path. The AOTF allows the free adjustment of the wavelength of the incident light between  $\lambda = 420$  nm and  $\lambda = 700$  nm. The output of the AOTF is linearly polarized however the polarization is lost after the transmission through a single mode fibre (FD7 FC/PC, NKT Photonics A/S). The quasi-monochromatic light illuminates the sample with a collimated beam under the initial polar angle  $\theta_1 = 122^\circ$  and azimuthal angle  $\varphi_1 = 341^\circ$  as defined in Fig. 2. These angles are chosen in such manner that no reflected light enters the detection path. The scattered light is collected by a long distance objective (LD-EC Epiplan-Neofluar 50x/0.55 HD DIC M27 air, Carl Zeiss AG) with an effective numerical aperture of  $\text{NA}_{\text{eff}} = 0.53$ . Thus, the acceptance angle is  $\theta_{\text{acc}} = 32^\circ$ , which yields the collection of scattered light between  $\theta = 89^\circ$  and  $\theta = 153^\circ$ .

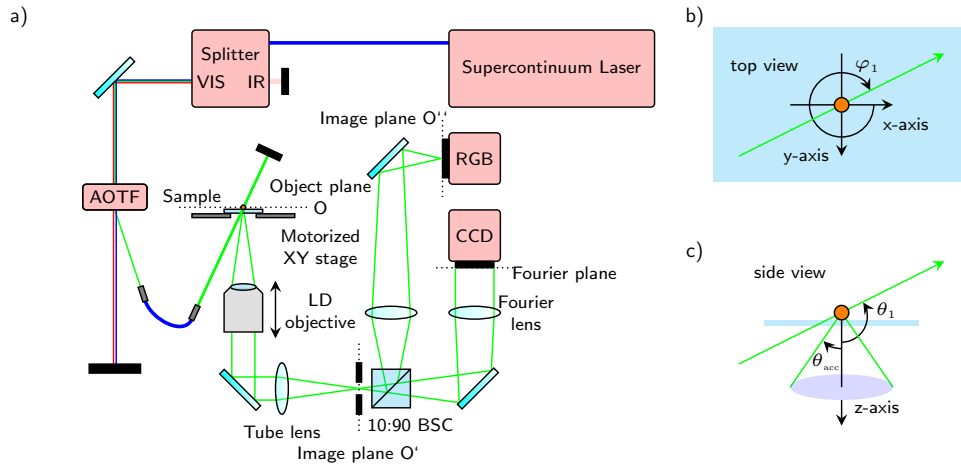


Fig. 2. **a)** The scattering microscope setup used in this work. An RGB camera enables the control of the exact position of the scatterer in respect to a pinhole which is used to eliminate undesired scattered light from contaminations on the sample. **b)** and **c)** Setup coordinate system.  $\varphi_1$  and  $\theta_1$  denote the angles between the incident light and the axes of the coordinate system. The scatterer is depicted as a circle in all pictures.

The back focal plane of the objective represents the Fourier transform of the scattered light, which is detected by a CCD camera (SIS p1010, Theta System GmbH), on which the Fourier plane is projected. The resolution is approximately  $0.2^\circ/\text{pixel}$ . By introducing a pinhole to the detection path in the image plane  $O'$  one can furthermore control the CCD camera's field of view and limit the spatial area which contributes to the scattered light on the detector.

### 2.2.1. Measurements

Angularly resolved measurements on printed microscatterers were performed with the scatterers still positioned on the glass substrate of the printing procedure. Non-spherical scatterers were rotated in such manner that the incident beam of light was perpendicular to their long axis (rod-like scatterers) or directly shining onto one of their faces (cubes). For the angularly resolved measurements a wavelength of  $543 \pm 3$  nm at full width half maximum (FWHM) was chosen. A pinhole was used to cut off scattered light from contaminations on the sample which would otherwise distort the scattering images as discussed in Müller *et al* [34].

For further utilisation, such as correlation evaluation with theoretical data, the angular measurements were interpolated on a 400 by 400 points grid, the background was subtracted and the data normalized to its maximum. The interpolation was done using a native Matlab function, namely the `TriScatterInterp()` (MATLAB, R2013b, MathWorks) function. The correlation with theoretical data was calculated with

$$C_\lambda(r, n_s) = \frac{\text{Cov}[I_{T,\lambda}(\theta, \varphi, r, n_s), I_{E,\lambda}(\theta, \varphi)]}{\sqrt{\text{Var}[I_{T,\lambda}(\theta, \varphi, r, n_s)]}\sqrt{\text{Var}[I_{E,\lambda}(\theta, \varphi)]}}, \quad (1)$$

where  $I_{T,\lambda}$  are the theoretically obtained intensity values at a certain wavelength  $\lambda$  and  $I_{E,\lambda}$  are the experimental values.

### 2.3. Atomic force microscopy (AFM)

AFM measurements were performed on a NanoWizard 4 AFM (NanoWizard 4 Bioscience AFM, JPK BioAFM Center, Bruker Nano GmbH) with silicon cantilevers (ACTA Probe, Applied NanoStructures, Inc.). The cantilever has a nominal spring constant of 37 N/m and a typical tip radius of 6 nm. Measurements were carried out in tapping mode and the post processing of the measurements was done using Gwyddion, an open source software for SPM data analysis [35]. Artefacts like tilt and flawed lines were corrected and the data was smoothed by applying a Gaussian filter.

## 3. Results

To explore the possibilities of manufacturing microparticles with a 3D-DLW system we first created relatively simple geometric objects and examined their scattering behaviour. For the printing parameters a scan speed of  $5000 \mu\text{m/s}$  and a laser power of 30 % were chosen. According to Guney *et al* [33] this results in a voxel diameter of approximately  $0.25 \mu\text{m}$  and a voxel height of approximately  $0.5 \mu\text{m}$ . These dimensions were taken into account during the model generation, e.g. to obtain a truly spherical body the CAD-model needs to be an oblate spheroid. The printed particles were exclusively sliced with contour lines at 100 nm distance with the commercial software DeScribe (Nanoscribe GmbH, Germany).

### 3.1. Spheres

Spheres were chosen as scatterer geometry to investigate the feasibility of creating round features on a micron scale and because their scattering behaviour is well known. After the printing and washing procedure, the spheres remained on the glass substrate, where they also were examined. To check the printing parameters, AFM measurements were done in order to verify the roundness

of the spheres. After post processing of the AFM data, spheres were fitted on the data and profile lines were drawn in order to compare the spherical shape of the printed bodies to perfect spheres as shown in Fig. 3. The comparison of the AFM images with ideal spheres show good agreement with both the targeted size and also the shape of an ideal sphere, thus, demonstrating that the estimated voxel sizes of a single polymerization spot were correct. Except from the right edge, where the geometry of the used AFM tip caused larger deviations, the relative differences between the ideal and the printed sphere were mainly below 5 %.

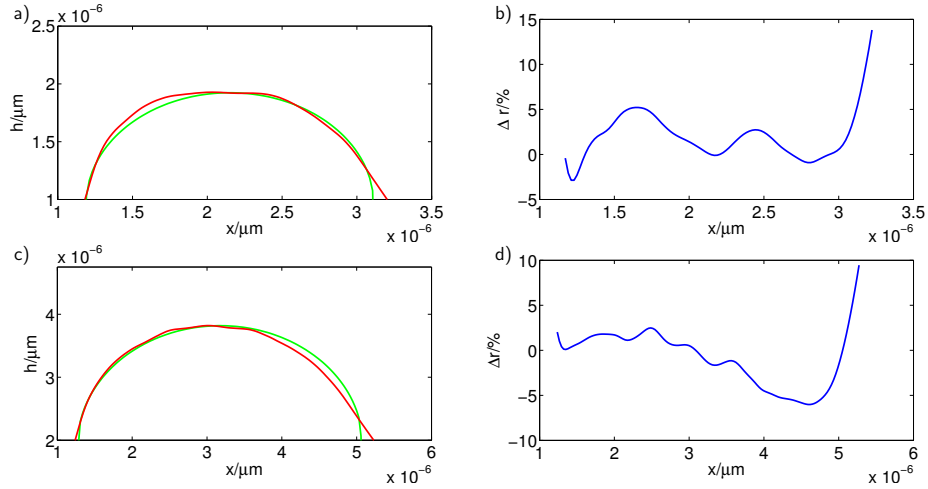


Fig. 3. **a)** and **c)** A profile of a printed sphere with targeted radius of  $r = 1 \mu\text{m}$  (red line) with a perfect sphere (green line) of radius  $r = 961 \text{ nm}$  and a printed sphere with targeted radius of  $r = 2 \mu\text{m}$  in comparison to a perfect sphere with  $r = 1.91 \mu\text{m}$ . **b)** and **d)** The relative deviation of the printed spheres from the respective ideal sphere using the aforementioned radii. Except for the flank on the right, where the deviations from the ideal sphere are caused by the geometry of the used AFM tip, the relative difference is mostly below 5 %.

Fig. 4a) and 4b) show a scanning electron microscope (SEM) image of a sphere with radii  $r = 1 \mu\text{m}$  and  $r = 5 \mu\text{m}$ , respectively. On the bigger sphere, the individual slicing layers are clearly visible as circular patterns, showing that the chosen printing parameters were not optimal for spheres having this size.

After the verification of the roundness of the scattering spheres with AFM measurements we compared the experimentally obtained scattering images with theoretical Mie calculations. Fig. 5 shows the experimental data as well as a theoretically calculated scattering image.

Spheres printed with the same parameters as the ones shown in Fig. 3 were examined with the scattering microscope at a wavelength of  $\lambda = 543 \text{ nm}$ , and correlated (see eq. (1)) with Mie calculations (see Rothe *et al* [15]) for spheres with radii ranging between  $r = 0.75 \mu\text{m}$  and  $r = 1.25 \mu\text{m}$  (stepsize  $0.5 \text{ nm}$ ) and refractive indices between  $n_s = 1.46$  and  $n_s = 1.52$  (stepsize  $0.0001$ ). In Fig. 5 an experimentally obtained image is shown next to the corresponding theoretical image with the highest correlation. Although there are differences visible between the experimental result and the calculated scattering image, the method of correlating these two images to each other yields reasonable results. For this sphere the target radius was  $r = 1.0 \mu\text{m}$  and the correlation peaked at  $r = 1.0185 \mu\text{m}$ . The obtained refractive index was  $n_s = 1.4808$ . For bulk material the manufacturer has noted a refractive index of  $n_s = 1.48$  at  $780 \text{ nm}$  with an expected rise of  $0.02$  at polymerization. Gissibl *et al* [36] have determined the refractive index of polymerized bulk IP-L 780 at  $543 \text{ nm}$  with  $n_s = 1.5168$ . This difference is physically justified since differences in the refractive index between bulk material and micro particles are

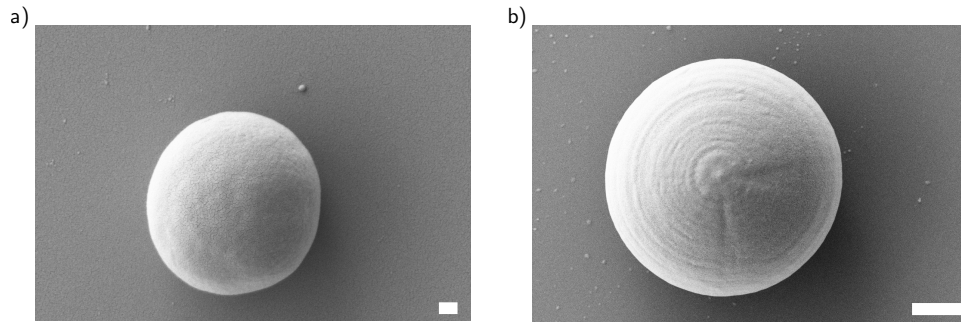


Fig. 4. **a)** SEM image of a sphere with target radius of  $r = 1 \mu\text{m}$ . The brittle surface is due to the coating which was applied in order to measure the spheres with the SEM and not from the printing process. **b)** Sphere with targeted radius of  $r = 5 \mu\text{m}$ . In contrast to the smaller sphere the individual layers are clearly visible. The scale bars are 200 nm and 2  $\mu\text{m}$ , respectively.

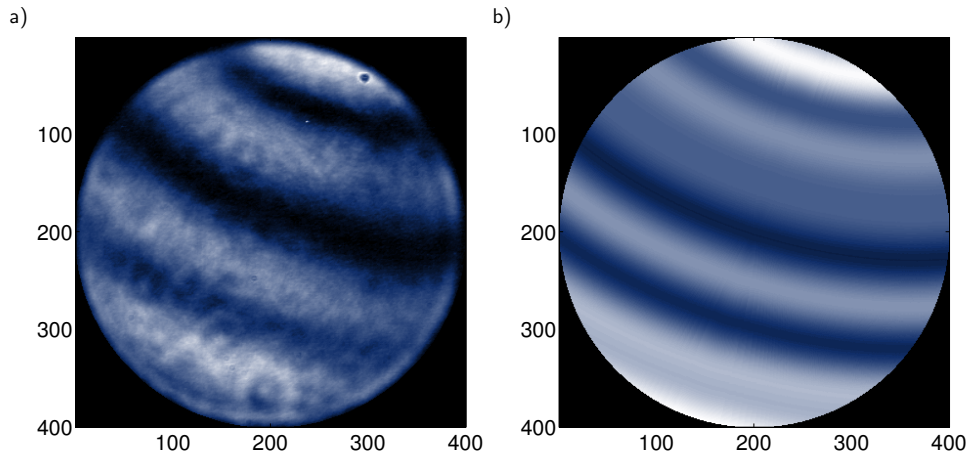


Fig. 5. **a)** Experimentally obtained image and **b)** the theoretical image with the highest correlation at  $r = 1.0185 \mu\text{m}$  with  $n_s = 1.4808$ . Even though the imperfection of the printed spheres is clearly visible in the scattering image the similarities are evident. Furthermore it shows the robustness of the correlation method which yields good results even for stronger deviating scattering images.

well reported [37,38]. Beyond that the refractive index changes whether the photo resist was polymerized with a 2PP process or UV-baking. Dottermusch *et al* [39] showed that the refractive index of the photo resist IP-Dip changed up to  $\Delta n = 0.01$  whether it was polymerized by 2PP or UV curing.

Fig. 6a) shows the measurement on a sphere with target radius  $r = 5 \mu\text{m}$  besides the calculated image with the highest correlation found at  $r = 5.0095 \mu\text{m}$ . Both the measurement and the theoretical pattern are plotted logarithmically to display all parts of the pattern equally good. As refractive index the previously obtained value of  $n_s = 1.4808$  was used and only the radius was varied between  $r = 4.75 \mu\text{m}$  and  $r = 5.25 \mu\text{m}$  in 0.5 nm steps. However, the deviation between the calculated pattern and the experimentally obtained image is larger than for the small sphere. This can maybe be explained by effects due to the decreasing surface quality.

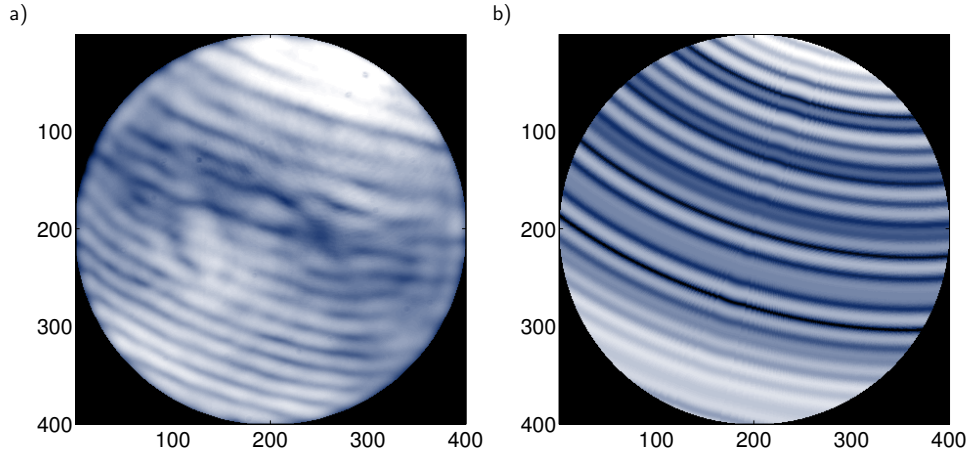


Fig. 6. **a)** Experimentally obtained image and **b)** the theoretical image, both plotted logarithmically, with the highest correlation at  $r = 5.0095 \mu\text{m}$ . The calculated image was obtained using the previously determined refractive image of  $n_s = 1.4808$ .

### 3.2. Cubes

The second type of scatterers with elementary geometry, which was examined in the present work, were cubes. Cubes were chosen in order to review the possibilities to create sharp edge-like features on a micron scale. However, there exists no analytical solution of Maxwell's equations for cubes, thus, an open source realization of the DDA method, namely the Amsterdam Discrete Dipole Approximation (ADDA [40]), was used to calculate the scattering patterns of the cubes.

During the measurements the cube was rotated in such manner that the  $\vec{k}_{xy}$  component of the incident light was perpendicular to one of the faces of the cube. The measurement conditions were recreated in the ADDA simulations, where a monochromatic, non-polarised, plane wave with a wavelength of 543 nm illuminated the cube under an initial polar angle of  $\theta_1 = 122^\circ$ . Due to its robustness and monotonic convergence, the conjugate gradient method (CGNR) [41] was chosen as iterative solver for all simulations. Scattering angles from  $\theta = 0^\circ$  to  $180^\circ$  were combined with azimuthal angles  $\varphi = 0^\circ$  to  $360^\circ$  in  $1^\circ$  steps to create an overview of the scattering pattern. For each angle pair a Mueller Matrix, describing the scattering behaviour for arbitrary polarisation under this angle, was calculated. Consequently the effects of the system such as polarisation changes due to the transition through the glass substrate can be handled in Mueller-Stokes calculus. Fig. 7a) shows the calculated overview of the whole solid angle for a cube with an edge length of  $2 \mu\text{m}$  and  $n_s = 1.4808$ . The marked area shows the angles which are detected in the scattering microscope and which are shown in detail in Fig. 7b). Fig. 7c) shows the experimentally obtained scattering image from a cube with the targeted edge length of  $2 \mu\text{m}$ . It may be expected that due to the finite voxel size it is impossible to achieve a cube with perfectly sharp edges. Nevertheless, the experimental result shows large similarity to the theoretical scattering pattern. Apart from the imperfect edges the remaining differences can be explained by effects due to tilt, which causes rotations and shifts of the scattering pattern. This has been discussed in detail by Müller *et al* [34].

The calculated and measured pattern of a cube with the edge length  $3 \mu\text{m}$  is presented in Fig. 8. The simulation was conducted using the afore determined refractive index of  $n_s = 1.4808$  and is very similar to the experimental image. Large cubic scatterers could be printed with good surface quality leading to a good agreement between the simulations and the measurements. Fig. 9 shows a SEM image with an overview as well as a close-up on cubes with an edge length

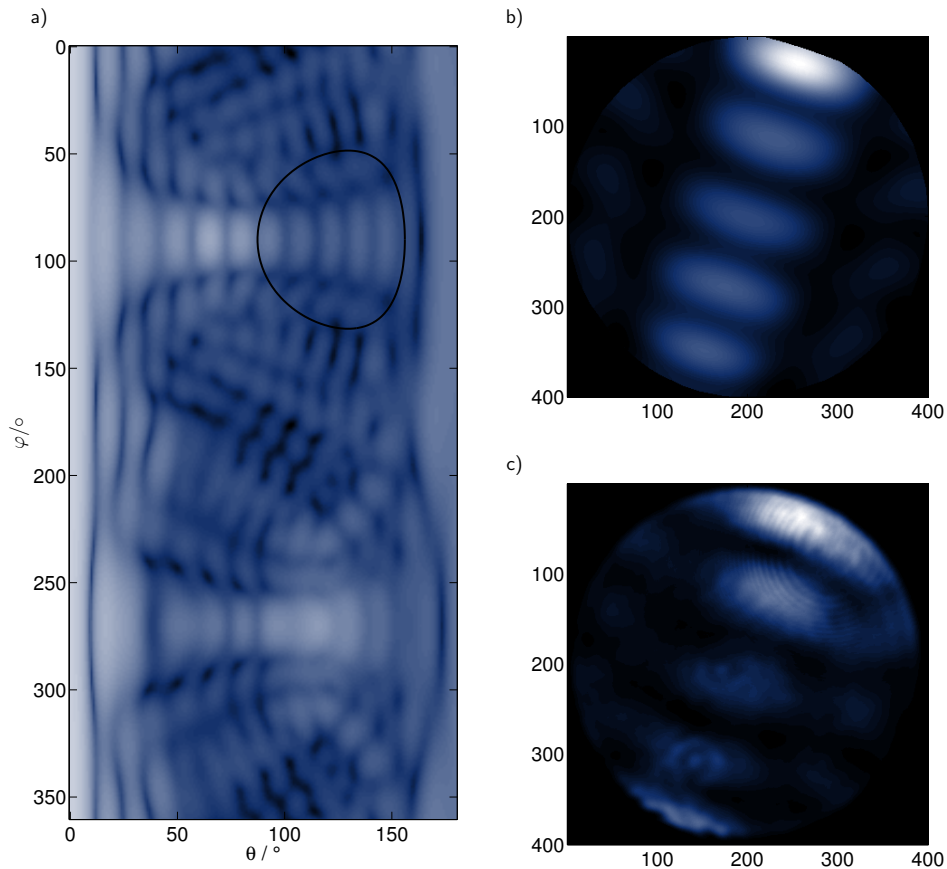


Fig. 7. **a)** Simulated light scattering view for the whole solid angle of a cube with edge length  $2\ \mu\text{m}$ . The overview is plotted logarithmically to better visualise the comparably low backscattering. **b)** Linearly plotted close-up of the scattering pattern, which is detected by the scattering microscope, represented by the marked area in Fig. 7a). **c)** Measured scattering image from a cube with targeted edge length of  $2\ \mu\text{m}$  plotted linearly. Minor deviations are visible, which are mostly caused by effects due to the rotation of the scatterer.

of  $10\ \mu\text{m}$ . This picture also shows how the orientation of the body during the printing process can affect the surface quality. While cubes resting on one of their faces seem to have a small bump on their upper surface, which is most likely caused by the decreasing length of the contour lines, the cubes which were printed standing on one of the corners do not exhibit this feature.

#### 4. Application

In the previous section it was shown that it is possible to fabricate round scattering bodies or such with edge-like features in a way that the resulting scattering images closely resemble the calculated scattering patterns for the corresponding ideal shapes.

As another possible application the present work examines the possibilities of using scattering bodies printed with the 3D-DLW system as phantoms for real non-spherical biological samples. As model organism *Escherichia coli* was chosen. The bacteria were modelled as cylinders with  $1\ \mu\text{m}$  diameter and hemispherical pole caps on both ends. Phantoms were printed with different lengths and examined with the scattering microscope and compared to measurements of a real *E. coli* bacterium.

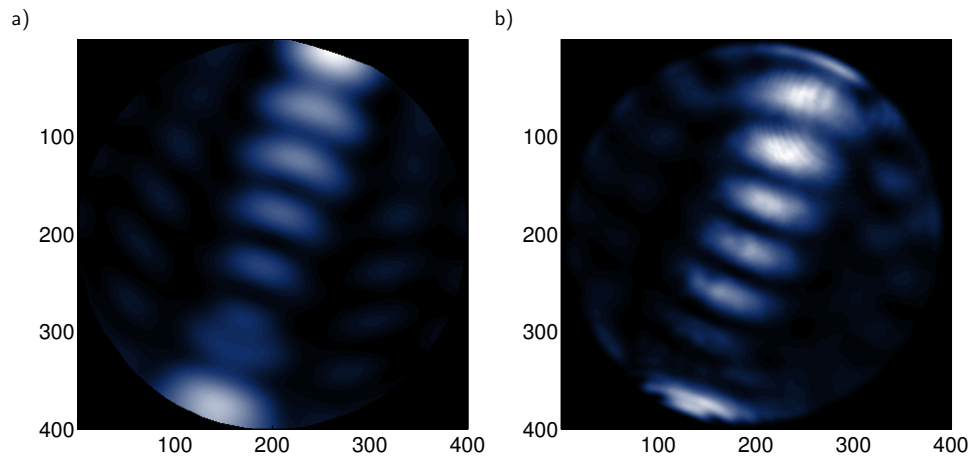


Fig. 8. **a)** Simulated pattern and **b)** the corresponding experimentally obtained scattering image of a cube with edge length 3  $\mu\text{m}$ , both plotted linearly. The simulation was again performed with the refractive index  $n = 1.4808$  and shows, apart from some minor deviations due to tilt, good similarity to the experimental image.

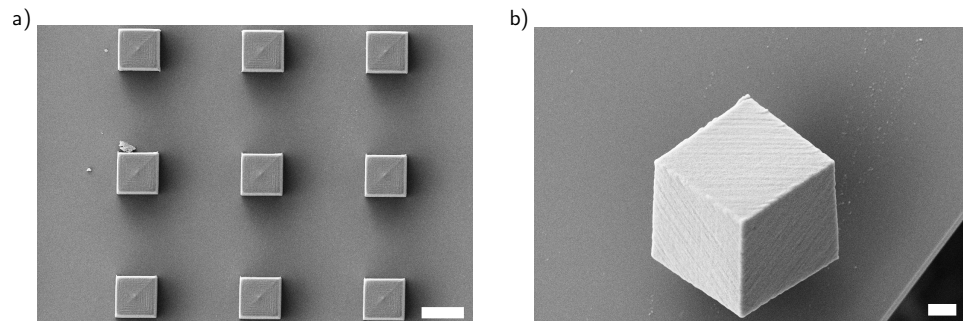


Fig. 9. **a)** SEM image showing an overview of cubes with an edge length of 10  $\mu\text{m}$ . Cubic scatterers have a good surface quality which results in good similarity between the simulations and experiments as shown in Figs. 7 and 8. **b)** Close-up of a 10  $\mu\text{m}$  cube which was printed standing on its tip. The orientation of the scatterer can affect the surface quality due to the layer-wise printing process. The scale bars in Fig. 7 and 8 are 10  $\mu\text{m}$  and 2  $\mu\text{m}$ , respectively.

Fig. 10 shows the obtained logarithmically plotted scattering images of a printed *E. coli* phantom (Fig. 10a) with a targeted length of 5  $\mu\text{m}$  and a real *E. coli* bacterium (Fig. 10b) of approximately the same length. *E. coli* in phosphate-buffered saline (PBS) were positioned on the same kind of glass substrate used in the 3D-DLW procedure and immediately measured after the PBS evaporated at room temperature. Both the phantoms and the real bacteria were aligned with their long axis perpendicular to the  $\vec{k}_{xy}$  component of the incident light beam. Apart from minor differences, due to small angle differences in positioning the samples towards the beam and the refractive index, the measurements show good agreement. Another source of the differences could be that, although the measurement was immediately performed after the evaporation of the PBS, effects due to flattening caused by dehydration cannot completely be excluded.

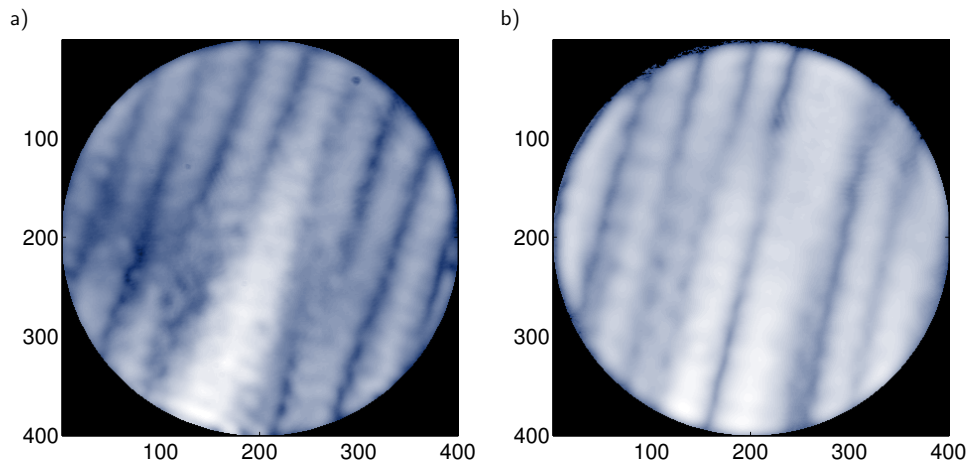


Fig. 10. **a)** Logarithmically plotted angularly resolved scattering image of a printed *E. coli* phantom with targeted length of  $5\ \mu\text{m}$  and **b)** logarithmically plotted scattering image of a real *E. coli* bacterium of approximately the same length.

## 5. Conclusion

The feasibility of fabricating microparticle phantoms with a 3D-DLW system was analysed and compared to simulations and measurements on actual microorganisms. The effects of the non-spherical voxels on the resulting microparticles' shape were shown to be partly compensated by factoring in the voxel size during the CAD-model generation. Hence, microbeads could be produced whose radii were shown to deviate less than 5 % from an ideal sphere. The theoretical validation of the ability to create sufficiently sharp edges showed no significant differences between the scattering patterns of an ideal cube and measurements of printed phantoms for this shape. Thus, the generation of any elementary shape is achievable. These printed bodies can be successfully used as phantoms for biological samples, as was shown for the case of *E. coli* bacteria.

While the used 3D-DLW system only reaches a lateral resolution of 200 nm, with corresponding height resolution between 400 and 500 nm, and larger, other 3D-DLW systems reach resolutions in the sub-100 nm regime. While we used our apparatus for the fabrication of micron scaled scatterers such as *E. coli* bacteria, above said 3D-DLW systems should be able to fabricate submicron scaled scatterers, e.g. viruses.

Further applications of this method could be the examination of larger scattering bodies. Obtaining structural information of an arbitrary scattering body from light scattering measurements is often achieved by correlation with numerical simulation results with a sweep of the optical or geometrical parameters. The parameters from the simulation yielding the highest correlation are assumed to be present during the measurement. However, single numerical simulations can take up to several hours, greatly rising with parameter dimensions, parameter range, and simulated volume. With the presented method it is possible to create an arbitrarily shaped scattering volume with  $20^3\ \mu\text{m}^3$  in several minutes. These scatterers can be produced with changing geometrical and optical parameters and subsequently measured in the actual experimental setup, thus replacing the numerical simulations and, additionally, the need to model the setup in the simulations. Arising differences due to the different refractive index can be countered by submerging the printed scatterers in index matching liquids to adjust their relative refractive index to that of the scatterer of interest.

Another possible application is the calibration of optical particle counters with non-spherical

particles. Particle counters are mainly calibrated with spherical polystyrene particles which causes errors for the size determination of particles with differing shape or refractive index. For the case of cubes with an edge length of 2  $\mu\text{m}$ , sliced and hatched with 100 nm distance and written with 5000  $\mu\text{m/s}$ , an output of approximately 6000 particles per hour can be achieved, which is very few compared to traditional manufacturing methods for microparticles such as the sol-gel procedure or top-down fabrication methods [42]. However, the strength of creating particles with the 3D-DLW lies in the short production cycle. It takes less than a day from the particle model to the printed particle, which allows fast adjustment of the particles with only little effort. Changing the size or shape of the produced particles does not come with additional costs, unlike with traditional approaches where templates and molds have to be manufactured before production. Furthermore, limitations to the shape are only given by the voxel shape and size. Additionally, by varying the laser power during the printing process optically heterogeneous particles are feasible. Thus, this method is ideally suited to rapid prototyping of particle designs. Custom-made particles offer a wide range of applications to many fields of research encouraging interdisciplinary collaboration. Therefore, the authors, whose main expertise is in the field of applied photonics, are open to future suggestions and cooperation utilizing custom-made particles in other fields of research.

## Acknowledgements

The work was funded by the DFG grant INST 40/500-1 FUGG to KEG. Furthermore the authors thank Florian Hausladen for the introduction to 3D-DLW and his support concerning the operation of the Photonic Professional GT as well as preparing the print files. The measurements with the SEM, which were performed by Manuel Mundsinger in the institute of Prof. Dr. Ute Kaiser, are acknowledged.

## References

1. C. Y. Young, P. J. Missel, N. A. Mazer, G. B. Benedek, and M. C. Carey, "Deduction of micellar shape from angular dissymmetry measurements of light scattered from aqueous sodium dodecyl sulfate solutions at high sodium chloride concentrations," *The J. Phys. Chem.* **82**, 1375–1378 (1978).
2. M. Schmitz, T. Rothe, and A. Kienle, "Evaluation of a spectrally resolved scattering microscope," *Biomed. optics express* **2**, 2665–2678 (2011).
3. H. Fang, L. Qiu, E. Vitkin, M. M. Zaman, C. Andersson, S. Salahuddin, L. M. Kimerer, P. B. Cipolloni, M. D. Modell, B. S. Turner *et al.*, "Confocal light absorption and scattering spectroscopic microscopy," *Appl. optics* **46**, 1760–1769 (2007).
4. J. Stark, T. Rothe, S. Kieß, S. Simon, and A. Kienle, "Light scattering microscopy measurements of single nuclei compared with gpu-accelerated ftd simulations," *Phys. Medicine & Biol.* **61**, 2749 (2016).
5. W. Bickel and M. Stafford, "Polarized light scattering from biological systems: a technique for cell differentiation," *J. Biol. Phys.* **9**, 53–66 (1981).
6. B. V. Bronk, S. D. Druger, J. Czege, and W. Van De Merwe, "Measuring diameters of rod-shaped bacteria in vivo with polarized light scattering," *Biophys. journal* **69**, 1170–1177 (1995).
7. Y. Jo, J. Jung, M.-h. Kim, H. Park, S.-J. Kang, and Y. Park, "Label-free identification of individual bacteria using fourier transform light scattering," *Opt. express* **23**, 15792–15805 (2015).
8. V. Backman, R. Gurjar, K. Badizadegan, I. Itzkan, R. R. Dasari, L. T. Perelman, and M. S. Feld, "Polarized light scattering spectroscopy for quantitative measurement of epithelial cellular structures in situ," *IEEE J. Sel. Top. Quantum Electron.* **5**, 1019–1026 (1999).
9. I. Itzkan, L. Qiu, H. Fang, M. M. Zaman, E. Vitkin, I. C. Ghiran, S. Salahuddin, M. Modell, C. Andersson, L. M. Kimerer *et al.*, "Confocal light absorption and scattering spectroscopic microscopy monitors organelles in live cells with no exogenous labels," *Proc. Natl. Acad. Sci.* **104**, 17255–17260 (2007).
10. A. Wax, C. Yang, V. Backman, K. Badizadegan, C. W. Boone, R. R. Dasari, and M. S. Feld, "Cellular organization and substructure measured using angle-resolved low-coherence interferometry," *Biophys. journal* **82**, 2256–2264 (2002).
11. Y. Liu, X. Li, Y. L. Kim, and V. Backman, "Elastic backscattering spectroscopic microscopy," *Opt. letters* **30**, 2445–2447 (2005).
12. A. Amelink, M. P. Bard, S. A. Burgers, and H. J. Sterenborg, "Single-scattering spectroscopy for the endoscopic analysis of particle size in superficial layers of turbid media," *Appl. optics* **42**, 4095–4101 (2003).

13. F. K. Forster, A. Kienle, R. Michels, and R. Hibst, "Phase function measurements on nonspherical scatterers using a two-axis goniometer," *J. Biomed. Opt.* **11**, 024018 (2006).
14. H. Ding, Z. Wang, F. Nguyen, S. A. Boppart, and G. Popescu, "Fourier transform light scattering of inhomogeneous and dynamic structures," *Phys. review letters* **101**, 238102 (2008).
15. T. Rothe, M. Schmitz, and A. Kienle, "Angular and spectrally resolved investigation of single particles by darkfield scattering microscopy," *J. Biomed. Opt.* **17**, 117006 (2012).
16. W. Cottrell, J. Wilson, and T. Foster, "Microscope enabling multimodality imaging, angle-resolved scattering, and scattering spectroscopy," *Opt. letters* **32**, 2348–2350 (2007).
17. G. Mie, "Beiträge zur Optik trüber Medien, speziell kolloidaler Metallösungen," *Annalen der physik* **330**, 377–445 (1908).
18. A. Taflovie and S. C. Hagness, *Computational electrodynamics: the finite-difference time-domain method* (Artech house, 2005).
19. B. T. Draine and P. J. Flatau, "Discrete-dipole approximation for scattering calculations," *JOSA A* **11**, 1491–1499 (1994).
20. S. Stolnik, L. Illum, and S. Davis, "Long circulating microparticulate drug carriers," *Adv. drug delivery reviews* **16**, 195–214 (1995).
21. B. Y. Liu, R. N. Berglund, and J. K. Agarwal, "Experimental studies of optical particle counters," *Atmospheric Environ.* (1967) **8**, 717–732 (1974).
22. Q. Wang, S. Fu, and T. Yu, "Emulsion polymerization," *Prog. Polym. Sci.* **19**, 703–753 (1994).
23. P. Foladori, A. Quaranta, and G. Ziglio, "Use of silica microspheres having refractive index similar to bacteria for conversion of flow cytometric forward light scatter into biovolume," *Water research* **42**, 3757–3766 (2008).
24. W. Stöber, A. Fink, and E. Bohn, "Controlled growth of monodisperse silica spheres in the micron size range," *J. colloid interface science* **26**, 62–69 (1968).
25. M. Antonietti, S. Lohmann, and C. Van Niel, "Polymerization in microemulsion. 2. surface control and functionalization of microparticles," *Macromolecules* **25**, 1139–1143 (1992).
26. S. Bhaskar, K. M. Pollock, M. Yoshida, and J. Lahann, "Towards designer microparticles: simultaneous control of anisotropy, shape, and size," *Small* **6**, 404–411 (2010).
27. J. A. Champion, Y. K. Katare, and S. Mitragotri, "Making polymeric micro-and nanoparticles of complex shapes," *Proc. Natl. Acad. Sci.* **104**, 11901–11904 (2007).
28. J. L. Perry, K. P. Herlihy, M. E. Napier, and J. M. DeSimone, "Print: a novel platform toward shape and size specific nanoparticle theranostics," *Accounts chemical research* **44**, 990–998 (2011).
29. Y. He and K. Park, "Effects of the microparticle shape on cellular uptake," *Mol. pharmaceutics* **13**, 2164–2171 (2016).
30. J. Wang, J. Coburn, C.-P. Liang, N. Woolsey, J. C. Ramella-Roman, Y. Chen, and T. J. Pfefer, "Three-dimensional printing of tissue phantoms for biophotonic imaging," *Opt. letters* **39**, 3010–3013 (2014).
31. T. Kairn, S. Crowe, and T. Markwell, "Use of 3d printed materials as tissue-equivalent phantoms," in *World Congress on Medical Physics and Biomedical Engineering, June 7-12, 2015, Toronto, Canada*, (Springer, 2015), pp. 728–731.
32. M. Farsari and B. N. Chichkov, "Materials processing: Two-photon fabrication," *Nat. photonics* **3**, 450 (2009).
33. M. Guney and G. Fedder, "Estimation of line dimensions in 3d direct laser writing lithography," *J. Micromechanics Microengineering* **26**, 105011 (2016).
34. D. Müller, D. Geiger, J. Stark, and A. Kienle, "Angle-resolved light scattering of single human chromosomes: experiments and simulations," *Phys. medicine biology* (2019).
35. D. Nečas and P. Klapetek, "Gwyddion: an open-source software for spm data analysis," *Open Phys.* **10**, 181–188 (2012).
36. T. Gissibl, S. Wagner, J. Sykora, M. Schmid, and H. Giessen, "Refractive index measurements of photo-resists for three-dimensional direct laser writing," *Opt. Mater. Express* **7**, 2293–2298 (2017).
37. F. Garcia-Santamaria, H. Miguez, M. Ibisate, F. Meseguer, and C. Lopez, "Refractive index properties of calcined silica submicrometer spheres," *Langmuir* **18**, 1942–1944 (2002).
38. Z. Hu and D. C. Ripple, "The use of index-matched beads in optical particle counters," *J. research Natl. Inst. Standards Technol.* **119**, 674 (2014).
39. S. Dottermusch, D. Busko, M. Langenhorst, U. W. Paetzold, and B. S. Richards, "Exposure-dependent refractive index of nanoscribe ip-dip photoresist layers," *Opt. letters* **44**, 29–32 (2019).
40. M. A. Yurkin, V. P. Maltsev, and A. G. Hoekstra, "The discrete dipole approximation for simulation of light scattering by particles much larger than the wavelength," *J. Quant. Spectrosc. Radiat. Transf.* **106**, 546–557 (2007).
41. R. Barrett, M. W. Berry, T. F. Chan, J. Demmel, J. Donato, J. Dongarra, V. Eijkhout, R. Pozo, C. Romine, and H. Van der Vorst, *Templates for the solution of linear systems: building blocks for iterative methods*, vol. 43 (Siam, 1994).
42. T. J. Merkel, K. P. Herlihy, J. Nunes, R. M. Orgel, J. P. Rolland, and J. M. DeSimone, "Scalable, shape-specific, top-down fabrication methods for the synthesis of engineered colloidal particles," *Langmuir* **26**, 13086–13096 (2009).